



# Initiation and evolution of urban-induced precipitation under different background wind speeds: Roles of urban breeze circulation and cold pool

Seong-Ho Hong<sup>1</sup> · Han-Gyul Jin<sup>2,3</sup> · Ji-Young Han<sup>4</sup> · Jong-Jin Baik<sup>1</sup>

Received: 27 November 2023 / Accepted: 15 September 2024 / Published online: 30 September 2024  
© The Author(s) 2024

## Abstract

Urban-enhanced precipitation is often observed far downwind of cities, suggesting important roles of background wind. This study examines the impacts of background wind on the initiation and evolution of urban-induced precipitation through idealized ensemble large-eddy simulations with different initial background wind speeds of 0, 1, 2, 3, 4, and 5 m s<sup>-1</sup>. Without background wind, a strong urban breeze circulation (UBC) initiates a relatively large number of cumulus clouds in the urban area, which exhibit greater cloud top heights than those in the rural area. The early-initiated clouds do not produce precipitation but moisten the middle troposphere, assisting later-initiated clouds to develop into deep convective clouds and produce concentrated precipitation in the urban area. As the background wind speed increases, the UBC weakens. Also, the high-humidity area generated by early-initiated clouds is continuously advected away from the urban area. Consequently, the precipitation initiation is delayed as the background wind speed increases. Precipitating clouds are advected downwind and generate a cold pool, and updrafts are repeatedly produced at the downwind boundary of the cold pool. The downwind-adverted clouds are fed by the newly produced updrafts, being a long-lived organized precipitation system that produces a considerable amount of precipitation in the downwind area. This feeding effect is most prominent for a moderate background wind (3 m s<sup>-1</sup>), causing the precipitation amount and duration to be maximized. For stronger background winds, precipitation is initiated by the mechanical lifting of the warm air of the urban boundary layer over the cool rural boundary layer around sunset.

**Keywords** Urban-induced precipitation · Background wind · Urban breeze circulation · Cold pool · Large-eddy simulation

## 1 Introduction

Urban areas have distinct surface characteristics as their surface is largely covered by manmade materials rather than natural vegetation. The heterogeneities in surface characteristics between urban and surrounding rural areas cause

thermal and dynamical differences in the air above which induce mesoscale circulations and/or perturb regional flows (e.g., Wong and Dirks 1978; Hidalgo et al. 2008; Dou et al. 2015). The induced circulations and/or perturbed flows may generate updrafts and initiate moist convection, leading to urban-induced precipitation (e.g., Thielen et al. 2000; Rozoff et al. 2003; Han and Baik 2008; Sun et al. 2021). On the other hand, precipitation systems passing over urban areas can be bifurcated (Zhang et al. 2017; Dou et al. 2020), intensified (Zhong and Yang 2015; Zhang et al. 2018), or weakened (Lorenz et al. 2019), which is referred to as urban modification of precipitation.

Urban impacts on clouds and precipitation have been evidenced by observational data. Many studies have reported that cloud cover is higher in the urban area than in the surrounding rural area in the afternoon in warm seasons (e.g., Romanov 1999; Inoue and Kimura 2004; Theeuwes et al. 2019), which implies the urban enhancement of cloud

✉ Jong-Jin Baik  
jjbaik@snu.ac.kr

<sup>1</sup> School of Earth and Environmental Sciences, Seoul National University, Seoul 08826, South Korea

<sup>2</sup> Department of Atmospheric Sciences, Pusan National University, Busan 46241, South Korea

<sup>3</sup> Institute for Future Earth, Pusan National University, Busan 46241, South Korea

<sup>4</sup> Korea Institute of Atmospheric Prediction Systems, Seoul 07071, South Korea

formation and development. Through a meta-analysis of 27 climatological observation studies of urban impacts on precipitation, Liu and Niyogi (2019) showed that precipitation is enhanced mainly in the urban areas (19% on average) and/or their downwind areas (22% on average). They reported that the downwind precipitation enhancement is prominent at a distance of 50 km (on average) from the urban center, which implies that the background wind may play important roles in urban impacts on precipitation. In addition, other features have also been identified: urban enhancement of precipitation pronounced in the late afternoon and evening in warm seasons (e.g., Balling and Brazel 1987; Burian and Shepherd 2005; Fujibe et al. 2009) and more frequent occurrence of heavy or short-and-heavy precipitation (e.g., Kishtawal et al. 2010; Yang et al. 2017; Wu et al. 2019; Jiang et al. 2020). These features are closely associated with urban-induced precipitation, often characterized by precipitation from relatively small convective systems formed by urban-induced circulations (e.g., Rozoff et al. 2003; Sun et al. 2021). Indeed, more frequent initiation of isolated convection is observed in urban areas compared to surrounding rural areas (e.g., Haberlie et al. 2015).

As possible explanations for the urban enhancement of precipitation, Changnon (1976; 1981) suggested the convection enhancement caused by urban heating and the low-level convergence caused by relatively rough urban surfaces. Through two-dimensional (2-D) idealized simulations where urban heating is specified by a bell-shaped distribution, Baik et al. (2001) showed that the updraft induced by the urban heat island (UHI) can initiate moist convection and produce precipitation in the downwind area in the presence of background wind. The follow-up study of Baik et al. (2007) indicates that the updraft induced by the UHI and the urban breeze circulation (UBC) is relatively strong when the boundary layer stability is low, which can explain the frequent occurrence of thunderstorms in the afternoon and evening. The important role of the UBC in urban-induced precipitation was also confirmed under realistic atmospheric conditions. Rozoff et al. (2003) simulated a heavy thunderstorm case in St. Louis, USA. They showed that the UBC plays a more important role in initiating thunderstorms than the local topography and urban roughness and that it leads to a precipitation increase downwind of St. Louis. Sun et al. (2021) conducted simulations in the Great Bay area, China, using the initial and lateral boundary conditions that were derived from a composite of localized extreme precipitation events. They showed that clouds are initiated by the UHI-induced low-level convergence and rapidly develop with an ample moisture supply by the background wind and sea breezes, producing a large amount of precipitation in the urban area mainly in the afternoon.

Although previous studies have shown that the dynamic forcing of the UBC can induce precipitation, there are

several aspects of urban-induced precipitation that still require more research. For example, the reasons why the largest precipitation enhancement is often observed in the distant downwind areas (e.g., Liu and Niyogi 2019) have not been revealed. Since the distant downwind areas are not under the direct influence of urban-induced thermal and dynamical forcings, how urban-induced precipitation systems are maintained as far as those areas and the roles of background wind in this regard deserve in-depth investigation. Also, it has not been investigated whether and how the urban-induced precipitation can occur under strong background wind conditions, to the authors' knowledge. Given that the UBC is relatively weak under strong background wind conditions (e.g., Zhang et al. 2014), another urban-related mechanism for triggering precipitation may exist, which will be investigated in this study. To investigate these aspects of urban-induced precipitation in the presence of background wind, a set of numerical simulations of urban-induced precipitation with different background wind speeds are needed. Here, because the initiation and evolution of urban-induced precipitation are closely associated with the diurnal variation of urban forcings, the urban forcings should be calculated considering various urban-related physical processes using a sophisticated urban canopy model, rather than being prescribed as a constant heating source as in previous studies (Baik et al. 2001; 2007; Han and Baik 2008).

Through the simulations of urban-induced precipitation under different background wind speeds, this study examines the roles of background wind in the initiation and evolution of urban-induced clouds and precipitation systems. Section 2 describes the experimental set-up. Section 3 presents the results and discussion. In Section 4, a summary and conclusions are given.

## 2 Experimental set-up

Idealized large-eddy simulations are conducted using the Weather Research and Forecasting (WRF) model version 4.1.3 (Skamarock et al. 2019). A 2-D (i.e.,  $x$ - and  $z$ -directions) domain with a horizontal extent of 500 km and a vertical extent of 20 km is used. The horizontal grid spacing is 100 m, and the vertical grid spacing is stretched from 60 to 241 m with 180 vertical layers being used. In the uppermost 5 km of the domain, Rayleigh damping is applied to prevent spurious reflections of gravity waves at the model top (Klemp et al. 2008). Periodic lateral boundaries are used. At the surface, a 20-km urban area is placed in the middle of the domain and the rest of the domain is set as a rural area. The urban area is comprised of a built-up portion (80%) and a natural portion (20%). In the built-up portion, urban surface parameters and diurnally varying anthropogenic heat flux are set following Ryu et al. (2013). In the natural portion of the

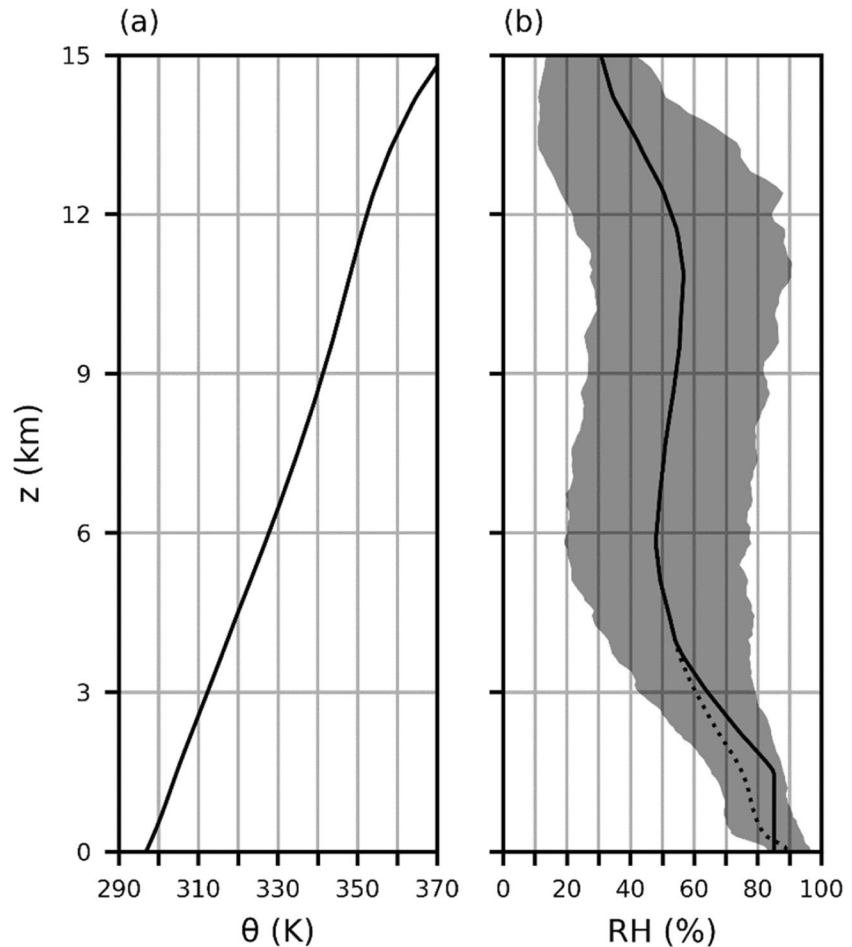
urban area, the land use type is set to a cropland-grassland mosaic with a vegetation fraction of 0.8 and the soil type is set to loamy sand. In the rural area, the land use type is set to a cropland-woodland mosaic with a vegetation fraction of 0.6 and the soil type is set to loamy sand.

The following physics parametrization schemes are used: the WRF double moment 6-class microphysics scheme (Lim and Hong 2010), the Dudhia shortwave radiation scheme (Dudhia 1989), the Rapid Radiative Transfer Model (RRTM) longwave radiation scheme (Mlawer et al. 1997), the unified Noah land surface model (Tewari et al. 2004), and the revised MM5 surface layer scheme (Jiménez et al. 2012). For turbulent mixing, the large-eddy simulation option with the prognostic turbulent kinetic energy closure is selected. To suppress the amplification of poorly resolved turbulent features with wavelengths of a few horizontal grid spacings, the sixth-order horizontal filter (Kniveton et al. 2007) is applied. The Seoul National University Urban Canopy Model (SNU-UCM; Ryu et al. 2011) is used for urban parametrization, being coupled with the unified Noah land surface model in a tile approach. Large-eddy simulations employing an urban canopy model enable simulating detailed flow characteristics with urban impacts being reliably reflected, which was

exemplified by several previous studies (e.g., Miao et al. 2011; Ryu et al. 2013; Zhang et al. 2022). The Coriolis effect is ignored in this study.

The simulations start at 0400 LST 15 August and end at 0500 LST 16 August (25 h) with a time step of 0.5 s. The latitude is set to 37.5°N which is the latitude of Seoul, South Korea. Accordingly, the sun rises at ~ 0530 LST and sets at ~ 1840 LST in the simulations. The initial vertical profiles of potential temperature and relative humidity are shown in Fig. 1. These initial vertical profiles are determined based on those from the European Centre for Medium-range Weather Forecasts (ECMWF) reanalysis 5 (ERA5) data (Hersbach et al. 2020) at the grid point closest to the center of Seoul at 0400 LST (UTC + 9). The ERA5 profiles are averaged for August over a period of 20 years (2003–2022) because August in South Korea is characterized by weak synoptic forcing, high surface temperature, and isolated convective showers, which indicate favorable conditions for urban-induced precipitation. Under these conditions, in August, large precipitation amounts were found in or downwind of Seoul (Hong et al. 2024). For the potential temperature, the mean ERA5 profile is used as it is, with random perturbations between −0.1 and 0.1 K at the three lowest levels. The

**Fig. 1** Vertical profiles of (a) initial potential temperature and (b) initial relative humidity (solid line) and ERA5 relative humidity at 0400 LST averaged for August over a period of 20 years (dotted line). The 25–75th percentile range of the ERA relative humidity at 0400 LST in August is shaded in gray



relative humidity is set to be constant at 85% within the lowest 1.5 km layer, and then it approaches linearly to the mean ERA5 profile to match it at  $z=4$  km. Above  $z=4$  km, the mean ERA5 profile is used as it is. The modified relative humidity profile is within the 25–75th percentile range of the individual ERA5 profiles (gray shade) at all altitudes, which indicates that the modified profile is acceptable to represent the humidity of August in Seoul (Fig. 1b). Six sets of simulations with different initial horizontal wind speeds ( $U_0$ ) of 0, 1, 2, 3, 4, and 5  $\text{m s}^{-1}$  are conducted. The initial horizontal wind is set to be vertically uniform from the surface to the model top, being directed to the positive  $x$ -direction. Each set of simulations with different background wind speeds is comprised of 10 ensemble members with different initial random perturbations on potential temperature, which is expected to give more robust results.

### 3 Results and discussion

#### 3.1 Precipitation characteristics

Figure 2 shows the ensemble-mean horizontal distributions of accumulated precipitation amount, ensemble-mean time series of domain-averaged precipitation rate, and ensemble-mean domain-averaged accumulated precipitation amount with different  $U_0$ . We apply a 5-km moving average to the ensemble-mean horizontal distribution and a 15-min moving average to the ensemble-mean time series. As  $U_0$  increases from 0 to 4  $\text{m s}^{-1}$ , precipitation tends to be distributed farther downwind and over a wider area, with a decreasing tendency in maximum accumulated precipitation amount (Fig. 2a). Note the considerable precipitation amounts in the downwind area farther than 40 km from the urban center for  $U_0=3 \text{ m s}^{-1}$ , as well as the large precipitation amounts in or close to the urban area for  $U_0=0\text{--}1 \text{ m s}^{-1}$ . The areas with the significant precipitation are similar to the areas where precipitation enhancements due to urban effects have been documented in previous studies (Changnon et al. 1977; Liu and Niyogi 2019). The precipitation period is delayed as  $U_0$  increases from 0 to 4  $\text{m s}^{-1}$  (Fig. 2b). For example, precipitation occurs in the late afternoon and early evening for  $U_0=0 \text{ m s}^{-1}$  while it occurs in the late evening and late at night for  $U_0=4 \text{ m s}^{-1}$ . The  $U_0=5 \text{ m s}^{-1}$  case exhibits earlier precipitation period with less late-night precipitation than the  $U_0=4 \text{ m s}^{-1}$  case. The domain-averaged accumulated precipitation amount changes non-monotonically with background wind speed; it varies little from  $U_0=0$  to 2  $\text{m s}^{-1}$ , peaks for  $U_0=3 \text{ m s}^{-1}$ , and then decreases with increasing  $U_0$  from 3 to 5  $\text{m s}^{-1}$  (Fig. 2c). The  $U_0=4$  and 5  $\text{m s}^{-1}$  cases each have one ensemble member with no precipitation in the urban area and downwind part of the domain.

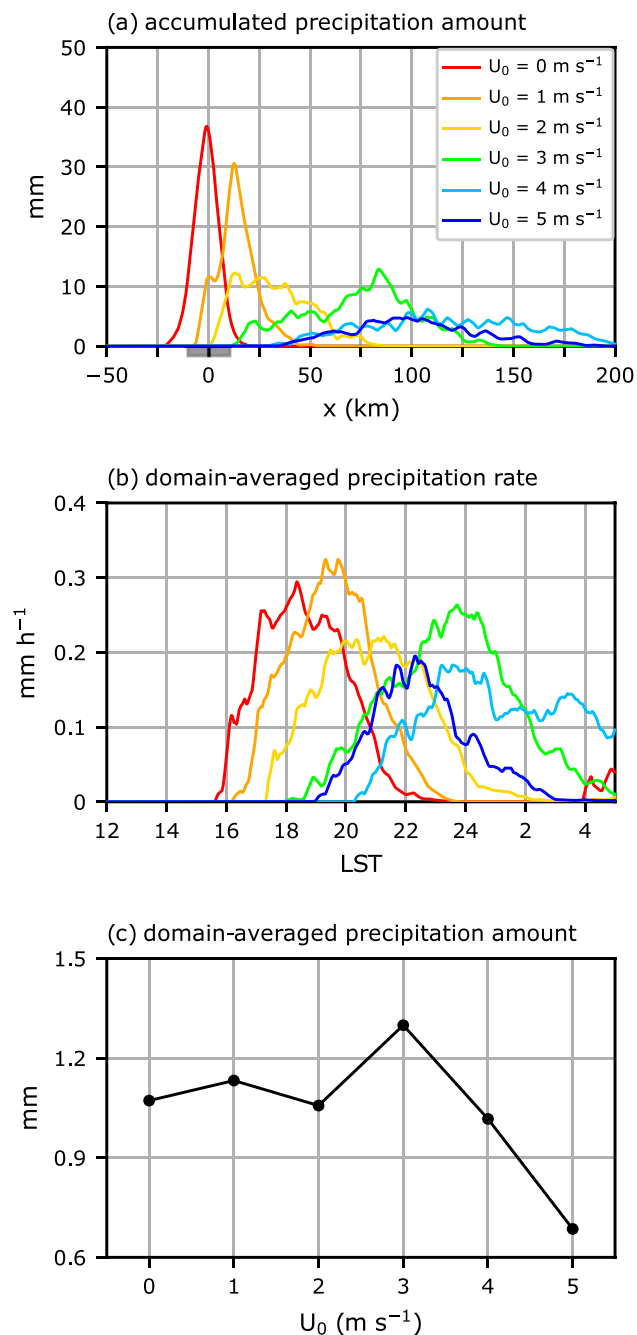
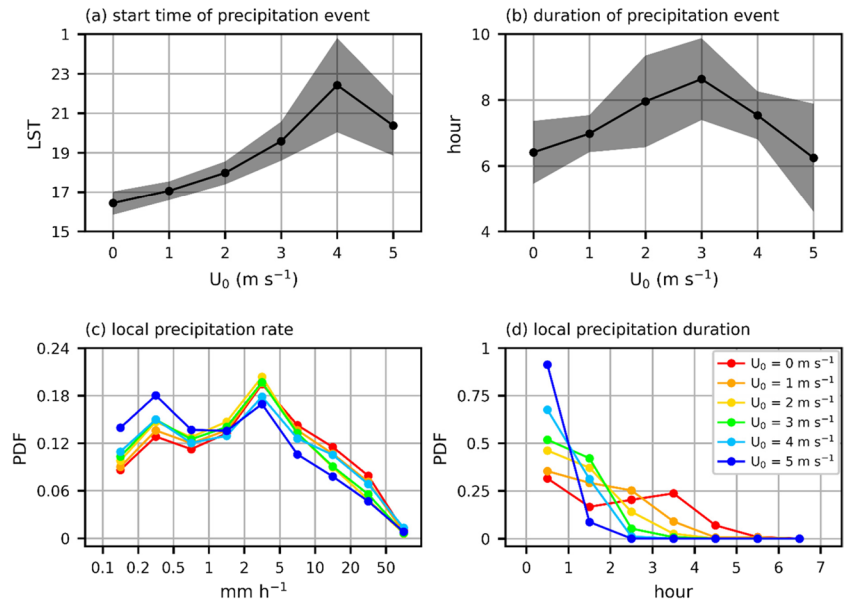


**Fig. 2** (a) Ensemble-mean horizontal distributions of accumulated precipitation amount, (b) ensemble-mean time series of domain-averaged precipitation rate, and (c) ensemble-mean domain-averaged accumulated precipitation amount with different  $U_0$ . The urban area is indicated by the gray box on the  $x$ -axis in (a)

Figures 3a and b show the ensemble means and spreads of start time and duration of precipitation event with different  $U_0$ . The start time of a precipitation event is calculated as the first time when the local precipitation rate exceeds 0.1  $\text{mm h}^{-1}$ , and the end time is calculated as the first time when the local precipitation rate decreases below

**Fig. 3** Ensemble means (black line) of (a) start time and (b) duration of precipitation event with different  $U_0$ . The  $\pm 1$  standard deviation range is shaded in gray to represent ensemble spreads. Ensemble-mean probability density functions of (c) local precipitation rate and (d) local precipitation duration with different  $U_0$



0.1  $\text{mm h}^{-1}$  after precipitation equivalent to half of the total accumulated precipitation has occurred. The duration of a precipitation event is calculated as the difference between the start and end times. The ensemble spread is represented by the range of  $\pm 1$  standard deviation of ensemble members. The onset of the precipitation event is delayed from  $\sim 1630$  to  $\sim 2230$  LST as  $U_0$  increases from 0 to  $4 \text{ m s}^{-1}$ . Although the precipitation onset for  $U_0 = 5 \text{ m s}^{-1}$  is earlier than that for  $U_0 = 4 \text{ m s}^{-1}$ , it is later than that for other  $U_0$ . The overall trend of delayed onset of precipitation with increasing background wind speed is qualitatively consistent with the results of Han and Baik (2008). The  $U_0 = 4$  and  $5 \text{ m s}^{-1}$  cases exhibit much larger spreads of the start time of the precipitation event (3–5 h) compared to the other cases (1–2 h). The duration of the precipitation event peaks for  $U_0 = 3 \text{ m s}^{-1}$ , similar to the domain-averaged accumulated precipitation amount (Fig. 2c); it increases from 6.4 to 8.6 h as  $U_0$  increases from 0 to  $3 \text{ m s}^{-1}$  and then decreases to 6.2 h as  $U_0$  further increases to  $5 \text{ m s}^{-1}$ . The ensemble-mean precipitation late at night for  $U_0 = 4 \text{ m s}^{-1}$  (Fig. 2b) is attributed to the late onset of precipitation in some ensemble members, rather than the overall longevity of precipitation (Figs. 3a and b).

The ensemble-mean probability density functions (PDFs) of local precipitation rate and duration with different  $U_0$  are shown in Figs. 3c and d. For the calculations of the PDFs, one-minute interval precipitation data at each grid point in the domain are used. The probability of heavy precipitation ( $> 10 \text{ mm h}^{-1}$ ) is substantial in general (13–20%), corresponding to 61–69% of total accumulated precipitation amount with different  $U_0$  (Fig. 3c). The local precipitation duration is mostly short ( $< 6 \text{ h}$ ) (Fig. 3d). The result that short and heavy precipitation accounts for a large portion of the induced precipitation is in accord with the observed

enhancements of short and heavy precipitation due to urban effects (Yang et al. 2017; Wu et al. 2019). The probability of heavy precipitation shows a decreasing tendency with increasing  $U_0$  except for  $U_0 = 4 \text{ m s}^{-1}$ , while that of light precipitation ( $< 1 \text{ mm h}^{-1}$ ) shows an increasing tendency with increasing  $U_0$ . The local precipitation duration tends to decrease as  $U_0$  increases. The changes in urban-induced precipitation with background wind speed are closely linked to the changes in the initiation and evolution of urban-induced clouds and precipitation systems which are examined in the following subsection.

### 3.2 Precipitation initiation: urban impacts

Figure 4a shows the ensemble-mean horizontal distributions of cloud cover averaged over the early afternoon (1200–1400 LST) with different  $U_0$ . The cloud cover at a grid point is set to one if the total water (liquid and ice) path is equal to or greater than  $0.01 \text{ kg m}^{-2}$ , otherwise it is set to zero. The ensemble-mean cloud cover at a grid point indicates a likelihood that the given grid point is covered by clouds. Overall, the cloud cover is relatively high in the urban area and its nearby areas compared to other rural area, which is qualitatively consistent with previous observations (Angevine et al. 2003; Inoue and Kimura 2004; Theeuwes et al. 2019). As  $U_0$  increases, the maximum cloud cover decreases and its location moves downwind from the urban center to the downwind edge of the urban area. To examine urban impacts on the temporal change of cloud cover, the urban-effect area is defined for each  $U_0$  (Table 1) as the 20-km area where the enhancement of cloud cover is evident. In this area, strong UHI and the central part of the UBC are also found (discussed later). The ensemble-mean time series of cloud

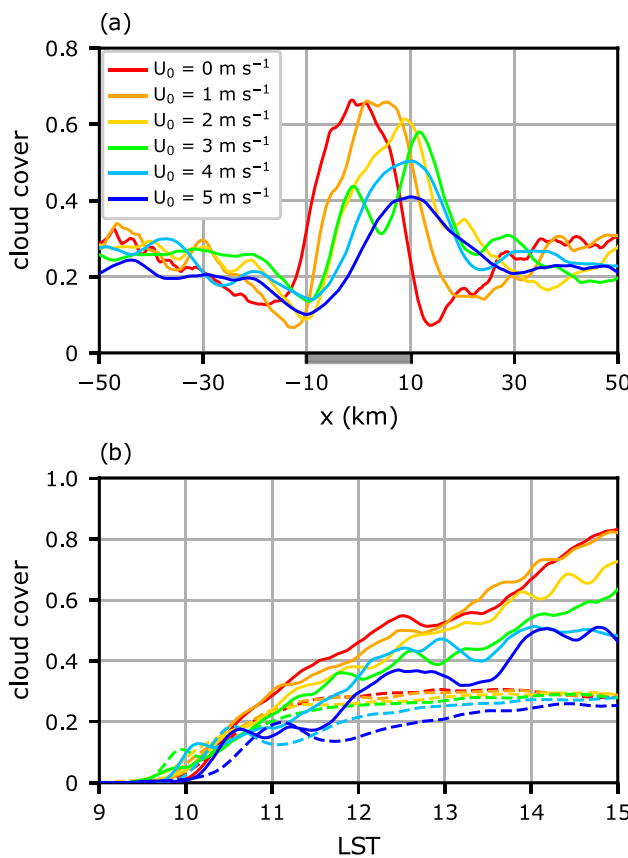


**Fig. 4** (a) Ensemble-mean horizontal distributions of cloud cover averaged over 1200–1400 LST and (b) ensemble-mean time series of cloud cover averaged over the urban-effect area (solid lines) and the rest of the domain (dashed lines) with different  $U_0$

**Table 1** Spatial range of the urban-effect area defined for different  $U_0$

$U_0 (\text{m s}^{-1})$	Urban-effect area
0	from $x = -10$ to 10 km
1	from $x = -6.7$ to 13.3 km
2	from $x = -3.3$ to 16.7 km
3, 4, 5	from $x = 0$ to 20 km

cover averaged over the urban-effect area and the rest of the domain with different  $U_0$  are presented in Fig. 4b. In areas outside of the urban-effect area, the cloud cover increases up to  $\sim 0.3$  until the late morning or early afternoon and then remains nearly unchanged. However, in the urban-effect area, the cloud cover continues to increase throughout the afternoon, exhibiting a slower increase for larger  $U_0$ .

The continuous increase in cloud cover in the urban-effect area during the afternoon is due to the UBC that continues to drive updrafts there. Figure 5 shows the fields of vertical velocity, horizontal velocity anomaly, and cloud water mixing ratio in a single ensemble member at 1300 LST

for  $U_0 = 0 \text{ m s}^{-1}$  and at 1500 LST for  $U_0 = 3 \text{ m s}^{-1}$ . The anomaly of a variable is calculated as the deviation from its horizontal average at each height. The UBC is apparent in both cases, but the location of the UBC center is different. It is located near the urban center for  $U_0 = 0 \text{ m s}^{-1}$  (Fig. 5a) and close to the downwind edge of the urban area for  $U_0 = 3 \text{ m s}^{-1}$  (Fig. 5b), being within the urban-effect area for each  $U_0$  (Table 1). Thermals ascend from the surface more frequently near the UBC center than in other areas in both cases. This leads to relatively many and high cumulus clouds in the urban area for  $U_0 = 0 \text{ m s}^{-1}$  and in the urban area and its nearby downwind area for  $U_0 = 3 \text{ m s}^{-1}$ , compared to the upwind and distant downwind areas (Figs. 5c and d). The UBC-induced abundance of clouds is qualitatively in line with the modeling results of Theeuwes et al. (2022). Note that the cumulus clouds formed near the UBC center remain in the urban area when the background wind is absent (Fig. 5c), while they are advected downwind and are spread horizontally when the background wind is present (Fig. 5d).

The background wind affects the intensity of the UHI that results from the difference in surface sensible heat flux between the urban and rural areas. Figures 6a and b show the ensemble-mean time series of urban–rural difference in surface sensible heat flux and potential temperature anomaly averaged over  $z = 0\text{--}0.5 \text{ km}$  in the urban-effect area. The potential temperature anomaly is used as a measure of UHI intensity. Until  $\sim 1100$  LST, the sensible heat flux difference is similar in all cases, increasing with time (Fig. 6a). However, in the afternoon, it exhibits different temporal changes with different  $U_0$ ; it tends to start decreasing earlier for smaller  $U_0$ . This is because for smaller  $U_0$ , the downward shortwave radiation at the surface starts decreasing earlier due to a faster increase in cloud cover in the urban area (Fig. 4b). Although the sensible heat flux difference in the early afternoon (1200–1300 LST) is larger for larger  $U_0$ , the UHI intensity in the early afternoon tends to be weaker for larger  $U_0$  because the increase in the dissipation effect on the UHI with increasing background wind speed is superior to the decrease in the cloud shadow effect.

The changes in the UHI intensity by background wind lead to the changes in the developments of the UBC and daytime cumulus clouds. Figures 6c and d show the ensemble-mean time series of the magnitude of horizontal velocity anomaly averaged over  $z = 0\text{--}0.5 \text{ km}$  in the urban-effect area and the maximum cloud top height between  $x = -20$  and 80 km with different  $U_0$ . The magnitude (i.e., absolute value) of horizontal velocity anomaly is used as a measure of UBC intensity. The cloud top height at each horizontal location is defined as the height at which the total water path integrated downward from the model top first exceeds  $0.1 \text{ kg m}^{-2}$  (Jung and Arakawa 2008). The UBC intensity generally increases with time in the late morning and early afternoon, as the

**Fig. 5** Fields of (**a, b**) horizontal velocity anomaly (shades) and (**c, d**) cloud water mixing ratio (shades) with vertical velocity (contours) in a single ensemble member (**a, c**) at 1300 LST for  $U_0 = 0 \text{ m s}^{-1}$  and (**b, d**) at 1500 LST for  $U_0 = 3 \text{ m s}^{-1}$ . The contours for vertical velocity are plotted at  $-6, -3, -1, 1, 3$ , and  $6 \text{ m s}^{-1}$ , and those of negative values are indicated by dashed lines. The location of the UBC center is indicated by the pink arrow. The urban area is indicated by the gray box on the  $x$ -axis

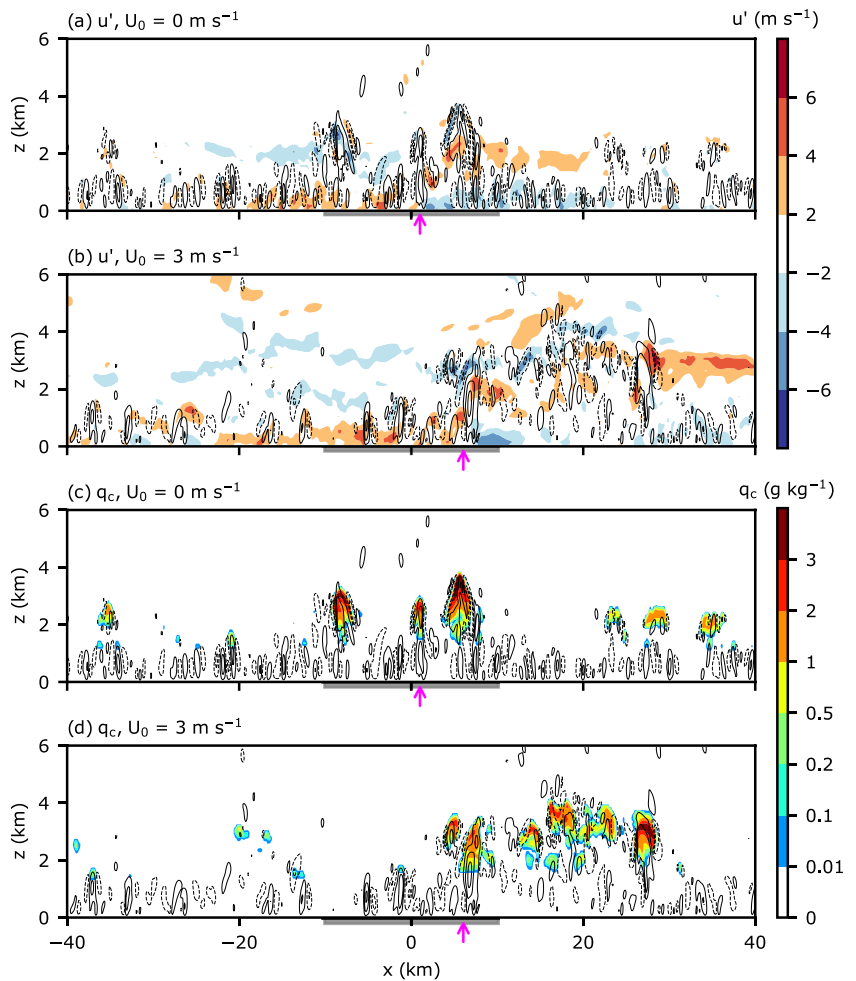
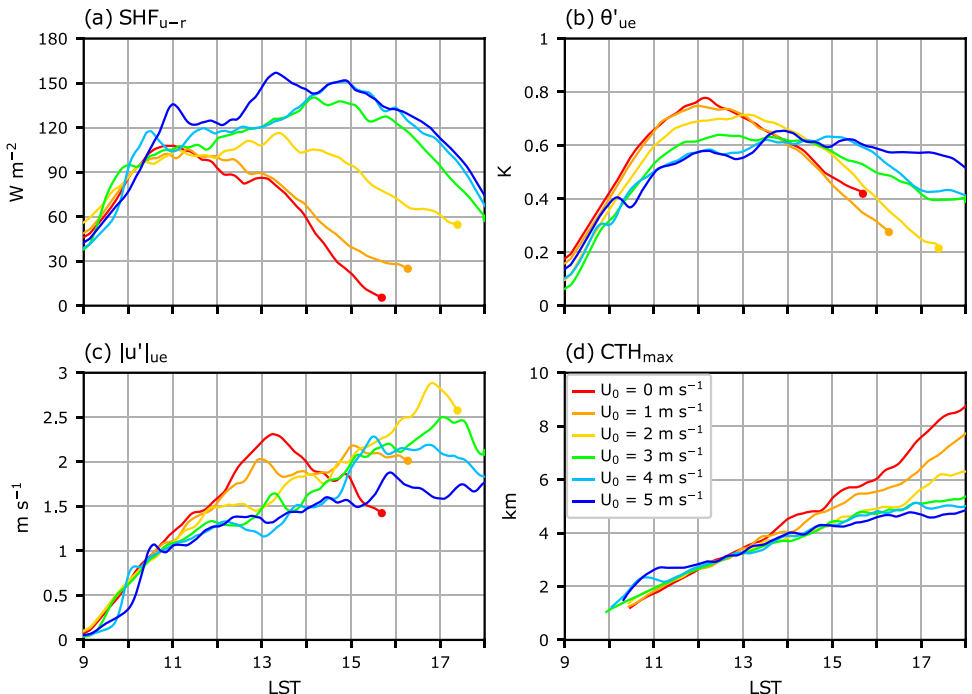


**Fig. 6** Ensemble-mean time series of (**a**) difference in surface sensible heat flux between the urban and rural areas, (**b**) potential temperature anomaly and (**c**) magnitude of horizontal velocity anomaly averaged over  $z = 0\text{--}0.5 \text{ km}$  in the urban-effect area, and (**d**) maximum cloud top height between  $x = -20$  and  $80 \text{ km}$  with different  $U_0$ . The time series in (**a**), (**b**), and (**c**) are plotted only until the earliest start time of precipitation among all ensemble members, to exclude the signals associated with precipitation-induced cold pools



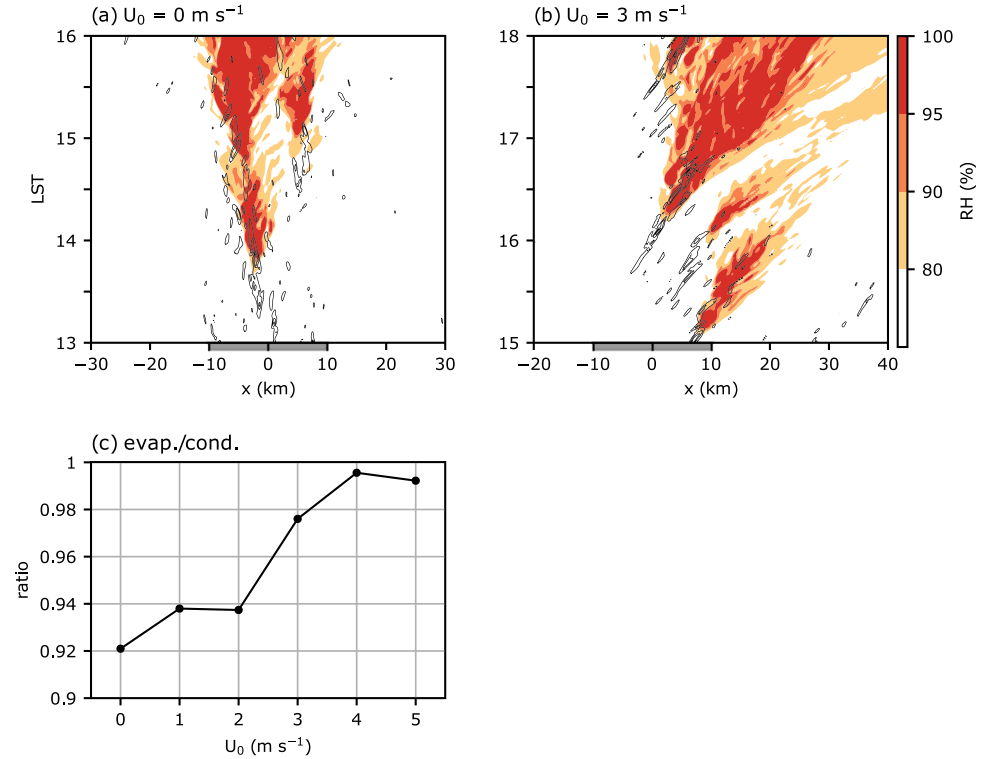
UHI intensity increases with time (Fig. 6c). Due to the weaker UHI intensity for larger  $U_0$ , the UBC intensity tends to increase more slowly with time and thereby be weaker for larger  $U_0$ . This leads to the slower development of cumulus clouds in the urban area or its nearby downwind area and therefore impedes the occurrence of deep convective clouds for larger  $U_0$  (Fig. 6d). Similar impacts of background wind were reported by Lee et al. (2019). Through the large-eddy simulations with prescribed heterogeneous surface sensible heat fluxes, they showed that the increase in background wind speed weakens the heterogeneity-induced mesoscale circulation and hinders the transition of cumulus clouds to deeper convection.

The background wind advects UBC-induced clouds downwind of the UBC, which also affects the development of these clouds. Figure 7 shows the distance–time plots of vertical velocity near the boundary layer top ( $z=1.5\text{--}2\text{ km}$ ) and relative humidity in the lower–middle troposphere ( $z=3\text{--}5\text{ km}$ ) in a single ensemble member for  $U_0=0$  and  $3\text{ m s}^{-1}$ , as well as the ratio of ensemble-mean evaporation rate to ensemble-mean condensation rate averaged between  $x=-20$  and  $80\text{ km}$  during 2 h as a function of  $U_0$ . The 2-h period used for the time average of evaporation and condensation rates differs depending on the  $U_0$  cases. In the  $U_0=0\text{--}2\text{ m s}^{-1}$  cases, the 2 hours before the earliest start time of precipitation for each  $U_0$  are used. In the  $U_0=3\text{--}5\text{ m s}^{-1}$  cases where the earliest precipitation occurs after 1800 LST (Fig. 3a), the 2 hours before 1800 LST are

used. The reason for using the period before 1800 LST is to confine analyses to the clouds induced by the UBC which weakens as sunset approaches. For  $U_0=0\text{ m s}^{-1}$ , thermals rising in the urban area from 1300 to 1410 LST produce cumulus clouds and moisten the lower–middle troposphere (Fig. 7a). While these thermals cannot rise higher than 6 km, the thermals generated below the moistened layer from  $\sim 1420$  LST rise higher, enabling the clouds to develop above  $z=6\text{ km}$ . This is qualitatively in line with the results of previous studies which indicate the role of preceding thermals in making subsequently generated thermals rise higher by moistening the middle troposphere (Waite and Khouider 2010; Moser and Lasher-Trapp 2017). However, for  $U_0=3\text{ m s}^{-1}$ , the clouds and moistened layer produced by the preceding thermals are advected downwind and the subsequently generated thermals rise in a relatively dry environment compared to those for  $U_0=0\text{ m s}^{-1}$  (Fig. 7b). As  $U_0$  increases, the condensates produced by the consecutively rising thermals tend to evaporate more (Fig. 7c) because they are more exposed to the relatively dry environment, which impedes the higher development of the UBC-induced clouds. Together with the contribution of UBC weakening (Fig. 6c), this effect plays an important role in the delay of precipitation initiation with increasing background wind speed (Fig. 3a).

For  $U_0=4$  and  $5\text{ m s}^{-1}$ , the ensemble-mean start time of precipitation is after 2030 LST (Fig. 3a) when the UBC that was developed in the daytime has already dissipated

**Fig. 7** Distance–time plots of vertical velocity averaged over  $z=1.5\text{--}2\text{ km}$  (contours) and relative humidity averaged over  $z=3\text{--}5\text{ km}$  (shades) in a single ensemble member for  $U_0=(\mathbf{a}) 0$  and  $(\mathbf{b}) 3\text{ m s}^{-1}$ . The contours for vertical velocity are plotted at 2, 4, and  $6\text{ m s}^{-1}$ . The urban area is indicated by the gray box on the  $x$ -axis. **(c)** Ratio of ensemble-mean evaporation rate to ensemble-mean condensation rate with different  $U_0$



after sunset, implying a precipitation-triggering mechanism other than the UBC. Figure 8 shows the fields of potential temperature and relative humidity at 1800 and 1900 LST in a single ensemble member for  $U_0=5 \text{ m s}^{-1}$ . The UBC weakens with sunset, and the last cloud system induced by the UBC dissipates without precipitation. As the UBC dissipates, the cooler air of the upwind rural boundary layer is advected downwind, causing the warmer air of the urban boundary layer to rise above the cooler rural boundary layer downwind of the urban area (Fig. 8a). The lifted warm air becomes saturated (Fig. 8b). New moist convection is triggered there with an aid of the convergence associated with the collision between the cool air from the upwind rural boundary layer and that from the downwind rural boundary layer (Figs. 8c and d). The triggered convection eventually leads to deep convective clouds and precipitation. This mechanism is responsible for precipitation initiation in the  $U_0=4$  and  $5 \text{ m s}^{-1}$  cases and in some ensemble members for  $U_0=3 \text{ m s}^{-1}$ . This result suggests that for strong background winds, the lifting of warm air of the urban boundary layer may induce precipitation when other pronounced mechanical forcings are absent. In the  $U_0=5 \text{ m s}^{-1}$  case,

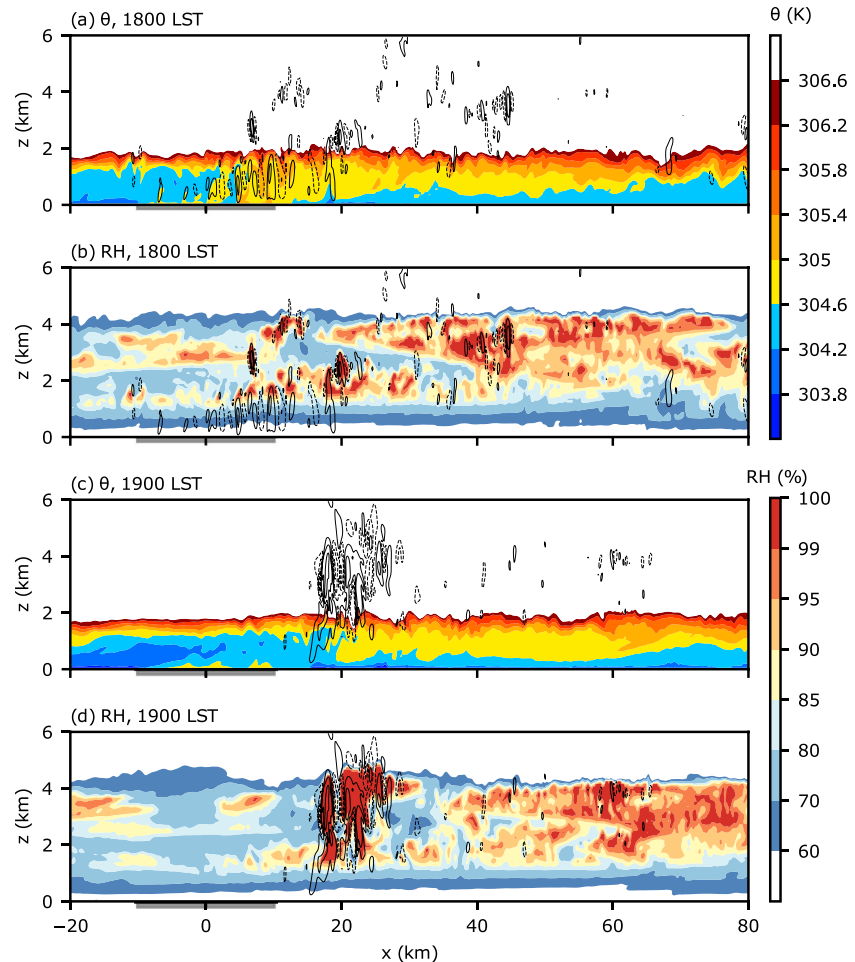
the UBC dissipates relatively early and the cool upwind air is advected downwind relatively fast compared to the  $U_0=4 \text{ m s}^{-1}$  case, leading to earlier lift of the warm air of the urban boundary layer (not shown). This allows for earlier initiation of precipitation for  $U_0=5 \text{ m s}^{-1}$  than for  $U_0=4 \text{ m s}^{-1}$  (Fig. 3a).

### 3.3 Precipitation system evolution: cold pool impacts

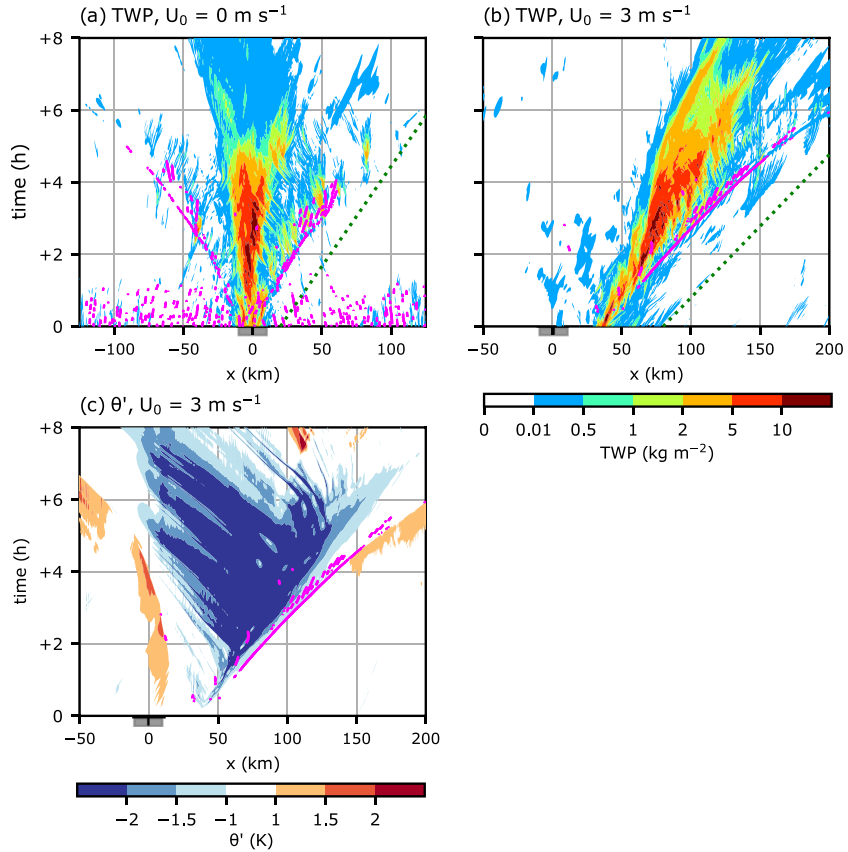
The UBC in the early afternoon is strongest and precipitation starts earliest for  $U_0=0 \text{ m s}^{-1}$ , with highly localized precipitation in and near the urban area. Meanwhile, the domain-averaged accumulated precipitation amount is largest for  $U_0=3 \text{ m s}^{-1}$ , with considerable precipitation over a wide downwind area. The reason why the domain-averaged precipitation amount is larger for  $U_0=3 \text{ m s}^{-1}$  than for  $U_0=0 \text{ m s}^{-1}$  where the strongest UBC appears is that cold pool impacts increase the lifetime of the precipitation system for  $U_0=3 \text{ m s}^{-1}$  but do not for  $U_0=0 \text{ m s}^{-1}$ .

Figure 9 shows the distance–time plots of total water path in a single ensemble member for  $U_0=0$  and  $3 \text{ m s}^{-1}$ , as well

**Fig. 8** Fields of (a, c) potential temperature (shades) and (b, d) relative humidity (shades) with vertical velocity (contours) at (a, b) 1800 and (c, d) 1900 LST in a single ensemble member for  $U_0=5 \text{ m s}^{-1}$ . The contours for vertical velocity are plotted at  $-6, -3, -1, 1, 3$ , and  $6 \text{ m s}^{-1}$ , and those of negative values are indicated by dashed lines. The urban area is indicated by the gray box on the  $x$ -axis



**Fig. 9** Distance–time plots of total water path (shades) in a single ensemble member for  $U_0$  = (a) 0 and (b)  $3 \text{ m s}^{-1}$ . The green dotted lines in (a) and (b) represent the moving speeds of 5 and  $7 \text{ m s}^{-1}$ , respectively. (c) Distance–time plot of potential temperature anomaly at  $z=0.1 \text{ km}$  (shades) in the same simulation for  $U_0=3 \text{ m s}^{-1}$ . The locations with horizontal convergence stronger than  $8 \times 10^{-3} \text{ s}^{-1}$  at  $z=0.1 \text{ km}$  are shaded in pink, and the urban area is indicated by the gray box on the x-axis



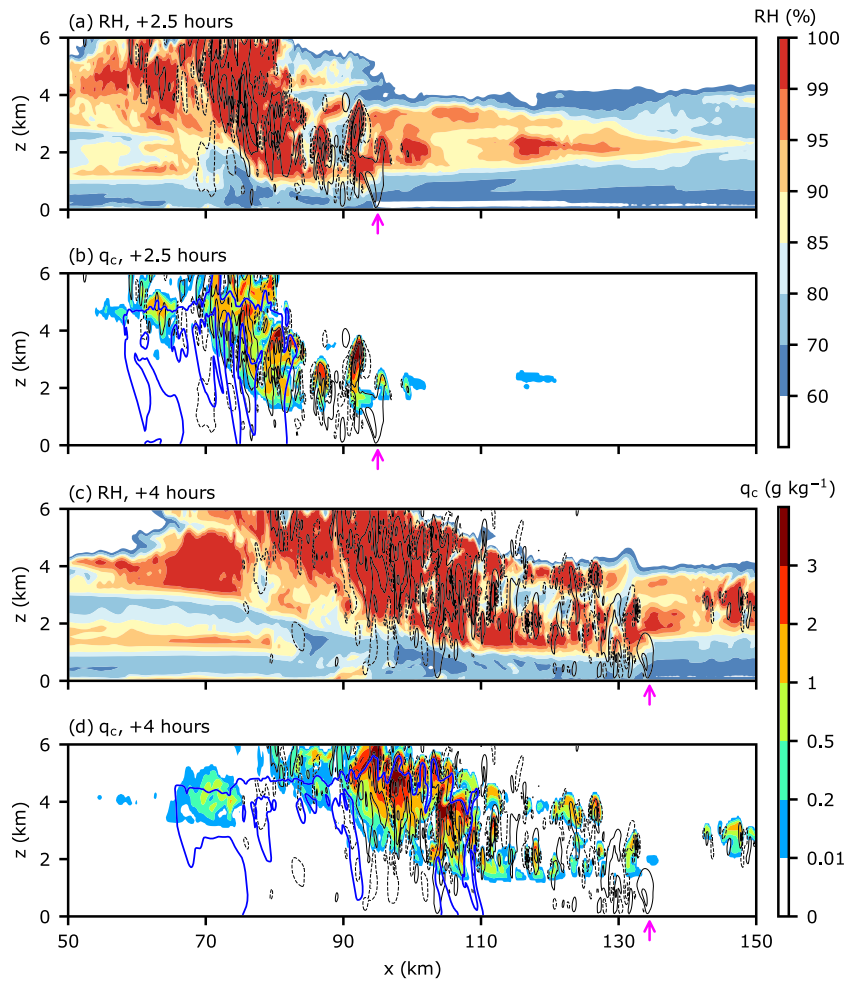
as the distance–time plot of potential temperature anomaly at  $z=0.1 \text{ km}$  for  $U_0=3 \text{ m s}^{-1}$ . The ordinate is the time after the precipitation onset. In general, precipitation systems have a size of meso- $\gamma$  or meso- $\beta$  scale. The precipitation system remains in the urban area and concentrates precipitation there when the background wind is absent (Fig. 9a), while it moves downwind and produces precipitation over a wider area when the background wind is present (Fig. 9b). The moving velocity of the system increases as  $U_0$  increases, which leads to a decrease in the local precipitation duration (Fig. 3d). After precipitation starts, a cold pool forms below the precipitation system (Fig. 9c). The moving velocity of the gust front characterized by strong horizontal convergence is about  $5 \text{ m s}^{-1}$  for  $U_0=0 \text{ m s}^{-1}$  and about  $7 \text{ m s}^{-1}$  for  $U_0=3 \text{ m s}^{-1}$  (Figs. 9a and b). New convective cells are generated by the gust front but soon dissipate for  $U_0=0 \text{ m s}^{-1}$ . However, for  $U_0=3 \text{ m s}^{-1}$ , the cells generated behind the gust front merge with the preexisting precipitation system, which produces an organized system and leads to a longer overall duration of precipitation.

To show the impacts of cold pool on the precipitation system in more detail, the fields of relative humidity, cloud water mixing ratio, and rain water mixing ratio 2.5 and 4 h after the precipitation onset in a single ensemble member for  $U_0=3 \text{ m s}^{-1}$  are presented in Fig. 10. At 2.5 h after the precipitation onset, the gust front is located about 10 km

downwind from the upper part ( $z \geq 4 \text{ km}$ ) of the precipitation system (Figs. 10a and b). The updrafts initiated by the gust front are advected upwind by front-to-rear flow, reach the upper part of the precipitation system, and play an important role in feeding the precipitation system. At 4 h after the precipitation initiation, the gust front is located farther downwind of the upper part of the precipitation system, so the updrafts initiated by the gust front are generally dissipated before reaching the upper part of the precipitation system as they pass through a relatively dry layer (Figs. 10c and d). The comparison between the  $U_0=0$  and  $3 \text{ m s}^{-1}$  cases (Figs. 9a and b) and the examination of role of cold pool (Fig. 10) suggest that the background wind can increase the lifetime of the urban-induced precipitation system through the feeding effect of the gust front, which enables the system to produce considerable precipitation (up to 13 mm) distant from the urban area.

The degree of feeding effect of the gust front on the precipitation system changes with background wind speed. Figure 11 shows the distance–time plots of total water path and the time series of rain water path averaged over a 250-km area in a single ensemble member for  $U_0=2, 3$ , and  $5 \text{ m s}^{-1}$ . The range of the x-axis in each of Figs. 11a, b, and c is the 250-km area used in averaging. The area where the relative humidity averaged over  $z=4\text{--}6 \text{ km}$  exceeds 85% (black contour) generally corresponds to the area that the upper part of

**Fig. 10** Fields of **(a, c)** relative humidity (shades) and **(b, d)** cloud water mixing ratio (shades) and rain water mixing ratio (blue contours) with vertical velocity (black contours) (**a, b**) 2.5 and (**c, d**) 4 h after the precipitation onset in a single ensemble member for  $U_0 = 3 \text{ m s}^{-1}$ . The contours for rain water mixing ratio are plotted at 0.01 and  $1 \text{ g kg}^{-1}$ . The contours for vertical velocity are plotted at  $-6, -3, -1, 1, 3$ , and  $6 \text{ m s}^{-1}$ , and those of negative values are indicated by dashed lines. The location of the gust front is indicated by the pink arrow



the precipitation system occupies. In the  $U_0 = 2 \text{ m s}^{-1}$  case, the distance between the upper part of the precipitation system and the gust front increases relatively rapidly with time compared to the  $U_0 = 3 \text{ m s}^{-1}$  case (Figs. 11a and b). Hence, the dissipation of the gust front-induced updrafts before reaching the upper part of the precipitation system occurs earlier, leading to an earlier start of a decreasing trend in rain water for  $U_0 = 2 \text{ m s}^{-1}$  than for  $U_0 = 3 \text{ m s}^{-1}$  (Fig. 11d). This indicates that the increase in the duration of precipitation events from  $U_0 = 0$  to  $3 \text{ m s}^{-1}$  (Fig. 3b) is attributed to the increase in the duration of this feeding effect which results from the increase in the moving velocity of the precipitation system from  $U_0 = 0$  to  $3 \text{ m s}^{-1}$ .

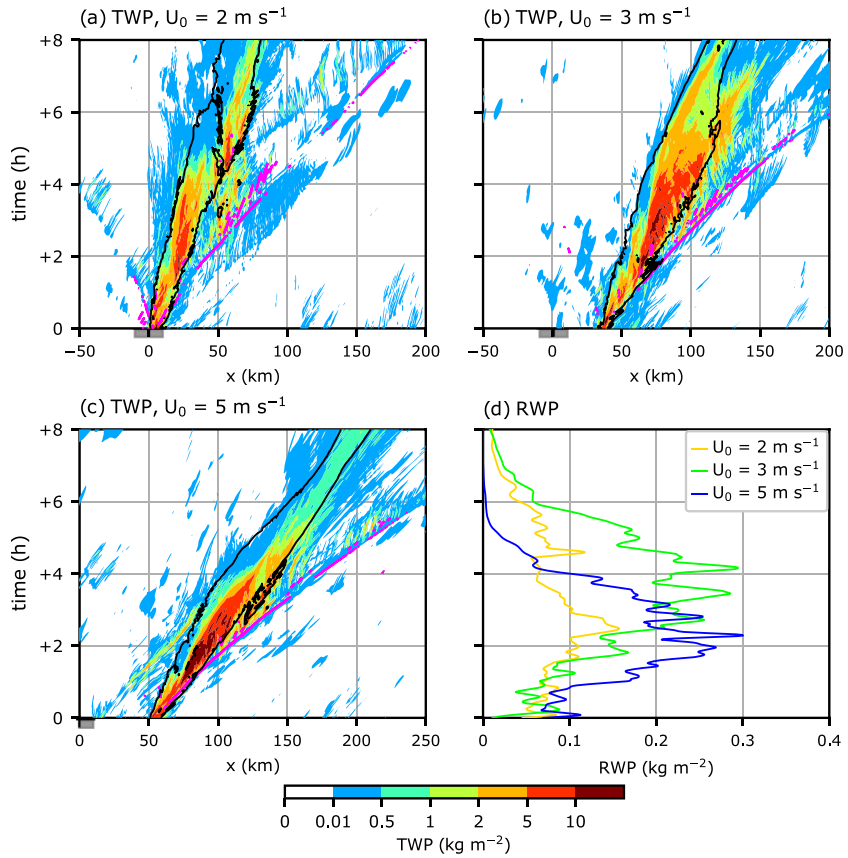
The lifetime of the precipitation system does not continue to increase with increasing background wind speed. The rain water in the precipitation system starts decreasing earlier for  $U_0 = 5 \text{ m s}^{-1}$  than for  $U_0 = 3 \text{ m s}^{-1}$  (Fig. 11d), although the upper part of the precipitation system moves faster and thereby is located closer to the gust front for  $U_0 = 5 \text{ m s}^{-1}$  than for  $U_0 = 3 \text{ m s}^{-1}$  (Figs. 11b and c). This is attributed in part to the earlier cessation of the updraft generation from the gust front for  $U_0 = 5 \text{ m s}^{-1}$  than for  $U_0 = 3 \text{ m s}^{-1}$ . Further

investigation of the factors that are crucial to the updraft generation from the gust front is needed, which is expected to improve our understanding of cold pool impacts on the lifetime of precipitation systems as many previous studies have done (e.g., Rotunno et al. 1988; Lin et al. 1998; Bryan et al. 2006). In some other ensemble members for  $U_0 = 5 \text{ m s}^{-1}$ , the dissipation of the weakly triggered precipitation system before the beginning of the feeding effect leads to the early end of precipitation, also contributing to the shorter ensemble-mean duration of precipitation events for  $U_0 = 5 \text{ m s}^{-1}$  than for  $U_0 = 3 \text{ m s}^{-1}$  (not shown).

#### 4 Summary and conclusions

In this study, we examined the initiation and evolution of urban-induced clouds and precipitation systems under different background wind speeds, to understand the role of background wind in urban-induced precipitation. Idealized ensemble large-eddy simulations with initial background wind speeds of 0, 1, 2, 3, 4, and  $5 \text{ m s}^{-1}$  were conducted under a summer condition. As the background wind speed

**Fig. 11** Distance–time plots of total water path (shades) with horizontal convergence stronger than  $8 \times 10^{-3} \text{ s}^{-1}$  at  $z=0.1 \text{ km}$  (pink shade) in a single ensemble member for  $U_0=(\mathbf{a}) 2, (\mathbf{b}) 3$ , and  $(\mathbf{c}) 5 \text{ m s}^{-1}$ . The area where the relative humidity averaged over  $z=4\text{--}6 \text{ km}$  is higher than 85% is indicated by the black contour. (**d**) Time series of rain water path averaged over a 250-km area in the same simulations



increases, the UBC weakens and the UBC-induced cumulus clouds are advected more rapidly downwind of the UBC center where updrafts rise repeatedly. Hence, the development of the UBC-induced clouds into deep convective clouds is impeded and the onset of precipitation is delayed, as the background wind speed increases. For strong background winds ( $U_0=4$  and  $5 \text{ m s}^{-1}$ ), the UBC-induced clouds end up dissipating without precipitation. Instead, the mechanical lifting of the warmer air of the urban boundary layer over the cooler rural boundary layer triggers a precipitation system around sunset. When the background wind is absent, the urban-induced precipitation system remains over the urban area, concentrating precipitation there. Meanwhile, when the background wind is present, the urban-induced precipitation system can be fed by the new updrafts produced from the downwind gust front of the cold pool, developing into an organized precipitation system. This feeding effect is most prominent for a moderate background wind ( $U_0=3 \text{ m s}^{-1}$ ), resulting in a precipitation system that lives long and produces a considerable amount of precipitation over a distant downwind area at this background wind speed.

The urban-induced precipitation simulated in this study generally features short duration, heavy intensity, and occurrence in the late afternoon or nighttime in the urban area or its downwind area, which are consistent with the

characteristics of observed urban precipitation enhancement. This supports that the simulations capture important aspects of the evolution of urban-induced precipitation systems in summer. Through detailed observations and simulations on the evolution of urban-induced precipitation systems, the roles of the urban boundary layer lifting and cold pool in the downwind precipitation need to be examined further.

The simulations in this study were conducted in a 2-D domain. This 2-D setting made multiple sets of large-eddy simulations feasible and facilitated understanding important physical processes. On the other hand, simulating clouds in a 2-D domain instead of a three-dimensional (3-D) domain can yield quantitative differences in entrainment and updraft/downdraft intensity, affecting cloud developments. Further investigation through 3-D simulations is needed. Although this study only considers an inland urban area without complex topography, many metropolitan cities have coastlines or mountains nearby. In such cities, the UBC can interact with other local circulations or topography-related flows. In addition, low-level temperature and humidity conditions in and around cities differ depending on synoptic weather and regional climate, affecting the development of urban-induced clouds. These aspects can complicate the impacts of background wind

on precipitation in cities and surrounding areas, deserving further investigation.

**Acknowledgements** The authors are grateful to two anonymous reviewers for providing valuable comments on this work. This work was supported by the National Research Foundation of Korea (NRF) under grant 2021R1A2C1007044. Han-Gyul Jin was supported by Global—Learning & Academic research institution for Master's-PhD students, and Postdocs (LAMP) Program of the National Research Foundation of Korea (NRF) grant funded by the Ministry of Education (No. RS-2023-00301938).

**Author contributions** J.-J. Baik designed this study. S.-H. Hong performed the data analysis and visualization. All authors discussed the results. S.-H. Hong wrote the original draft. H.-G. Jin, J.-Y. Han, and J.-J. Baik reviewed and edited the manuscript. All authors read and approved the final version of the manuscript.

**Data availability** The model simulation data in this study can be obtained from the corresponding author if necessary.

**Code availability** The codes used for analyses in this study can be obtained from the corresponding author if necessary.

## Declarations

**Conflict of interest** The authors declare no competing interests.

**Ethics approval** Not applicable.

**Consent to participate** Not applicable.

**Consent for publication** Not applicable.

**Open Access** This article is licensed under a Creative Commons Attribution-NonCommercial-NoDerivatives 4.0 International License, which permits any non-commercial use, sharing, distribution and reproduction in any medium or format, as long as you give appropriate credit to the original author(s) and the source, provide a link to the Creative Commons licence, and indicate if you modified the licensed material. You do not have permission under this licence to share adapted material derived from this article or parts of it. The images or other third party material in this article are included in the article's Creative Commons licence, unless indicated otherwise in a credit line to the material. If material is not included in the article's Creative Commons licence and your intended use is not permitted by statutory regulation or exceeds the permitted use, you will need to obtain permission directly from the copyright holder. To view a copy of this licence, visit <http://creativecommons.org/licenses/by-nc-nd/4.0/>.

## References

- Angevine WM, White AB, Senff CJ, Trainer M, Banta RM, Ayoub MA (2003) Urban–rural contrasts in mixing height and cloudiness over Nashville in 1999. *J Geophys Res* 108:4092
- Baik J-J, Kim Y-H, Chun H-Y (2001) Dry and moist convection forced by an urban heat island. *J Appl Meteorol* 40:1462–1475
- Baik J-J, Kim Y-H, Kim J-J, Han J-Y (2007) Effects of boundary-layer stability on urban heat island-induced circulation. *Theor Appl Climatol* 89:73–81
- Balling RC, Brazel SW (1987) Recent changes in Phoenix, Arizona summertime diurnal precipitation patterns. *Theor Appl Climatol* 38:50–54
- Bryan GH, Knievel JC, Parker MD (2006) A multimodel assessment of RKW theory's relevance to squall-line characteristics. *Mon Weather Rev* 134:2772–2792
- Burian SJ, Shepherd JM (2005) Effect of urbanization on the diurnal rainfall pattern in Houston. *Hydrol Process* 19:1089–1103
- Changnon SA (1976) Inadvertent weather modification. *Water Resour Res* 12:695–718
- Changnon SA (1981) Introduction. In: Changnon SA (ed) METROMEX: a review and summary. American Meteorological Society, Massachusetts, pp 1–16
- Changnon SA, Huff FA, Schickendantz PT, Vogel JL (1977) Summary of METROMEX, volume 1: weather anomalies and impacts. Illinois State Water Survey, Illinois
- Dou J, Wang Y, Bornstein R, Miao S (2015) Observed spatial characteristics of Beijing urban climate impacts on summer thunderstorms. *J Appl Meteorol Climatol* 54:94–105
- Dou J, Bornstein R, Miao S, Sun J, Zhang Y (2020) Observation and simulation of a bifurcating thunderstorm over Beijing. *J Appl Meteorol Climatol* 59:2129–2148
- Dudhia J (1989) Numerical study of convection observed during the Winter Monsoon Experiment using a mesoscale two-dimensional model. *J Atmos Sci* 46:3077–3107
- Fujibe F, Togawa H, Sakata M (2009) Long-term change and spatial anomaly of warm season afternoon precipitation in Tokyo. *SOLA* 5:17–20
- Haberlie AM, Ashley WS, Pingel TJ (2015) The effect of urbanization on the climatology of thunderstorm initiation. *Q J R Meteorol Soc* 141:663–675
- Han J-Y, Baik J-J (2008) A theoretical and numerical study of urban heat island-induced circulation and convection. *J Atmos Sci* 65:1859–1877
- Hersbach H, Bell B, Berrisford P, Hirahara S, Horányi A, Muñoz-Sabater J, Nicolas J, Peubey C, Radu R, Schepers D, Simmons A, Soci C, Abdalla S, Abellán X, Balsamo G, Bechtold P, Biavati G, Bidlot J, Bonavita M, Chiara GD, Dahlgren P, Dee D, Diamantakis M, Dragani R, Flemming J, Forbes R, Fuentes M, Geer A, Haimberger L, Healy S, Hogan RJ, Hólm E, Janisková M, Keeley S, Laloyaux P, Lopez P, Lupu C, Radnoti G, Rosnay PD, Rozum I, Vamborg F, Villaume S, Thépaut J-N (2020) The ERA5 global reanalysis. *Q J R Meteorol Soc* 146:1999–2049
- Hidalgo J, Pigeon G, Masson V (2008) Urban-breeze circulation during the CAPITOUL experiment: observational data analysis approach. *Meteorol Atmos Phys* 102:223–241
- Hong S-H, Jin H-G, Baik J-J (2024) Detection of urban effects on precipitation in the Seoul metropolitan area. *South Korea. Urban Clim* 53:101773
- Inoue T, Kimura F (2004) Urban effects on low-level clouds around the Tokyo metropolitan area on clear summer days. *Geophys Res Lett* 31:L05103
- Jiang X, Luo Y, Zhang D-L, Wu M (2020) Urbanization enhanced summertime extreme hourly precipitation over the Yangtze River Delta. *J Clim* 33:5809–5826
- Jiménez PA, Dudhia J, González-Rouco JF, Navarro J, Montávez JP, García-Bustamante E (2012) A revised scheme for the WRF surface layer formulation. *Mon Weather Rev* 140:898–918
- Jung J-H, Arakawa A (2008) A three-dimensional anelastic model based on the vorticity equation. *Mon Weather Rev* 136:276–294
- Kishtawal CM, Niyogi D, Tewari M, Pielke RA, Shepherd JM (2010) Urbanization signature in the observed heavy rainfall climatology over India. *Int J Climatol* 30:1908–1916
- Klemp JB, Dudhia J, Hassiotis AD (2008) An upper gravity-wave absorbing layer for NWP applications. *Mon Weather Rev* 136:3987–4004

- Knievel JC, Bryan GH, Hacker JP (2007) Explicit numerical diffusion in the WRF model. *Mon Weather Rev* 135:3808–3824
- Lee JM, Zhang Y, Klein SA (2019) The effect of land surface heterogeneity and background wind on shallow cumulus clouds and the transition to deeper convection. *J Atmos Sci* 76:401–419
- Lim K-SS, Hong S-Y (2010) Development of an effective double-moment cloud microphysics scheme with prognostic cloud condensation nuclei (CCN) for weather and climate models. *Mon Weather Rev* 138:1587–1612
- Lin Y-L, Deal RL, Kulie MS (1998) Mechanisms of cell regeneration, development, and propagation within a two-dimensional multicell storm. *J Atmos Sci* 55:1867–1886
- Liu J, Niyogi D (2019) Meta-analysis of urbanization impact on rainfall modification. *Sci Rep* 9:7301
- Lorenz JM, Kronenberg R, Bernhofer C, Niyogi D (2019) Urban rainfall modification: observational climatology over Berlin, Germany. *J Geophys Res: Atmos* 124:731–746
- Miao S, Chen F, Li Q, Fan S (2011) Impacts of urban processes and urbanization on summer precipitation: a case study of heavy rainfall in Beijing on 1 August 2006. *J Appl Meteorol Climatol* 50:806–825
- Mlawer EJ, Taubman SJ, Brown PD, Iacono MJ, Clough SA (1997) Radiative transfer for inhomogeneous atmospheres: RRTM, a validated correlated-k model for the longwave. *J Geophys Res* 102:16663–16682
- Moser DH, Lasher-Trapp S (2017) The influence of successive thermals on entrainment and dilution in a simulated cumulus congestus. *J Atmos Sci* 74:375–392
- Romanov P (1999) Urban influence on cloud cover estimated from satellite data. *Atmos Environ* 33:4163–4172
- Rotunno R, Klemp JB, Weisman ML (1988) A theory for strong, long-lived squall lines. *J Atmos Sci* 45:463–485
- Rozoff CM, Cotton WR, Adegoke JO (2003) Simulation of St. Louis, Missouri, land use impacts on thunderstorms. *J Appl Meteorol* 42:716–738
- Ryu Y-H, Baik J-J, Lee S-H (2011) A new single-layer urban canopy model for use in mesoscale atmospheric models. *J Appl Meteorol Climatol* 50:1773–1794
- Ryu Y-H, Baik J-J, Han J-Y (2013) Daytime urban breeze circulation and its interaction with convective cells. *Q J R Meteorol Soc* 139:401–413
- Skamarock WC, Klemp JB, Dudhia J, Gill DO, Liu Z, Berner J, Wang W, Powers JG, Duda MG, Barker DM, Huang X-Y (2019) A description of the advanced research WRF model version 4. National Center for Atmospheric Research, Colorado
- Sun X, Luo Y, Gao X, Wu M, Li M, Huang L, Zhang D-L, Xu H (2021) On the localized extreme rainfall over the Great Bay area in South China with complex topography and strong UHI effects. *Mon Weather Rev* 149:2777–2801
- Tewari M, Chen F, Wang W, Dudhia J, LeMone MA, Mitchell K, Ek M, Gayno G, Wegiel J, Cuenca RH (2004) Implementation and verification of the unified Noah land surface model in the WRF model. 20th conference on weather analysis and forecasting/16th conference on numerical weather prediction. Washington: American Meteorological Society
- Theeuwes NE, Boutle IA, Clark PA, Grimmond S (2022) Understanding London's summertime cloud cover. *Q J R Meteorol Soc* 148:454–465
- Theeuwes NE, Barlow JF, Teuling AJ, Grimmond CSB, Kotthaus S (2019) Persistent cloud cover over mega-cities linked to surface heat release. *npj Clim Atmos Sci* 2:15
- Thielen J, Wobrock W, Gadian A, Mestayer PG, Creutin J-D (2000) The possible influence of urban surfaces on rainfall development: a sensitivity study in 2D in the meso- $\gamma$ -scale. *Atmos Res* 54:15–39
- Waite ML, Khouider B (2010) The deepening of tropical convection by congestus preconditioning. *J Atmos Sci* 67:2601–2615
- Wong KK, Dirks RA (1978) Mesoscale perturbations on airflow in the urban mixing layer. *J Appl Meteorol* 17:677–688
- Wu M, Luo Y, Chen F, Wong WK (2019) Observed link of extreme hourly precipitation changes to urbanization over coastal South China. *J Appl Meteorol Climatol* 58:1799–1819
- Yang P, Ren G, Yan P (2017) Evidence for a strong association of short-duration intense rainfall with urbanization in the Beijing urban area. *J Clim* 30:5851–5870
- Zhang Y, Miao S, Dai Y, Bornstein R (2017) Numerical simulation of urban land surface effects on summer convective rainfall under different UHI intensity in Beijing. *J Geophys Res: Atmos* 122:7851–7868
- Zhang W, Villarini G, Vecchi GA, Smith JA (2018) Urbanization exacerbated the rainfall and flooding caused by hurricane Harvey in Houston. *Nature* 563:384–388
- Zhang W, Yang J, Yang L, Niyogi D (2022) Impacts of city shape on rainfall in inland and coastal environments. *Earth's Future* 10:e2022EF002654
- Zhang N, Wang X, Peng Z (2014) Large-eddy simulation of mesoscale circulations forced by inhomogeneous urban heat island. *Bound.-Layer Meteorol* 151:179–194
- Zhong S, Yang X-Q (2015) Mechanism of urbanization impact on a summer cold-frontal rainfall process in the Greater Beijing metropolitan area. *J Appl Meteorol Climatol* 54:1234–1247

**Publisher's Note** Springer Nature remains neutral with regard to jurisdictional claims in published maps and institutional affiliations.